

A Combined Spatial- and Frequency-Domain Interferometer for Sea Ice Thickness Measurement

¹Ziad A. Hussein, Benjamin Holt, Kyle C. McDonald,
Rolando Jordan, John Huang, Anhua Chu, Kyung Pak, Mike Gradziel

²Yasuo Kuga, Akira Ishimaru, Sermasak Jaruwatanadilok

³Prasad Gogineni, Torry Akins, Brandon Heavey

⁴Don Perovich, Matthew Sturm

¹Jet Propulsion Laboratory, California Institute of Technology, Pasadena, CA 91109

²University of Washington, Department of Electrical Engineering, Seattle, WA 98195

³University of Kansas, Department of Electrical Engineering, Lawrence, KA 66045

⁴US-Army Cold Region Research and Engineering Laboratory, Hanover, NH 03755

email: Ziad.A.Hussein@jpl.nasa.gov, Tel: 818 354-0533

Abstract— Thickness of Arctic sea ice plays a major role in Earth's climate and ocean circulation. An accurate measurement of this parameter on synoptic scales at regular intervals would provide a critical component for understanding the heat balance and air-sea-ice interactions which are keys for assessing the impacts of the changing polar climate. In this paper, we present new instrument technology for the remote sensing of sea ice thickness. This technology utilizes a combined spatial and frequency domain interferometric radar, providing angular and frequency correlation functions (ACF/FCF) between two radar waves with slightly differing VHF-band frequencies and incidence and observation angles. The sea ice thickness is derived from the interferometric phase of the ACF/FCF functions. This new instrument technology, the cryospheric advanced sensor (CAS), is currently being developed under the NASA/ESTO instrument incubator program (IIP). Designed for eventual implementation on a spacecraft, and the initial radar test-bed will be on a Twin Otter aircraft. The progress of several aspects of this project is presented

1. INTRODUCTION

The thickness of polar sea ice is an indicator of the state of ocean circulation and associated air-sea heat exchange within the Polar Regions, and can have profound impacts on the global heat balance and ocean thermohaline circulation. Measurements of sea ice thickness and associated snow cover characteristics are critical to understanding Earth's climate and ocean circulation. Thermodynamically, the comparatively thin sea ice and overlying snow cover reduce heat exchange between the ocean and atmosphere, strongly impact albedo during summer melt, and impact the fresh water flux out of the Arctic. The ice cover itself is impacted by wind and current forcing, forming ridges from undeformed ice and altering the ice mass volume.

Currently, ICESat (laser altimeter), EnviSAT (radar altimeter) and the upcoming CryoSAT (radar altimeter) measurement systems provide estimates of the sea ice freeboard, i.e. that portion of the ice that is above the sea level. The sea ice thickness and changes in thickness are inferred from these measurements. However, knowledge of freeboard allows only an indirect inference of sea ice thickness. Furthermore, the freeboard measurement requires considerable vertical measurement accuracy together with *a priori* information of snow cover depth in order to limit retrieval errors. Developing a means of determining sea ice

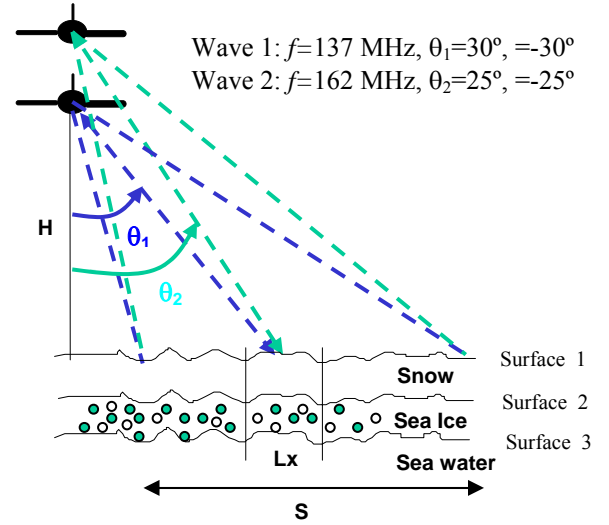


Figure 1. Geometry of combined spatial and frequency domain interferometer. L_x represents the resolution cell, and S the width of the illumination swath.

thickness directly and its overlying snow cover on broad, synoptic-scales at regular intervals would fill one of the highest priority science measurement gaps in the polar regions.

In this paper, we develop the theoretical basis and present a prototype instrument technology for application of radar interferometry in the VHF band to the direct estimation of sea ice thickness [1-7]. The medium is modeled as multi-layered stratification consisting of snow, sea ice (including spherical particles of air bubbles and brine inclusions), and sea water. Each surface interface (air-snow, snow-ice and ice-water) is modeled as a two-dimensional rough surface (3D geometry) with a Gaussian roughness spectrum. We utilize the angular and frequency correlation functions (ACF/FCF) of the electromagnetic wave scattered from sea ice medium, employing the small perturbation method (SPM) [1] and the Kirchhoff rough surface scattering and Rayleigh volume scattering models [2],[3]. The ACF/FCF is obtained by taking the correlation between two signals with different frequencies and incident angles, forming a combined spatial- and frequency-domain interferometer

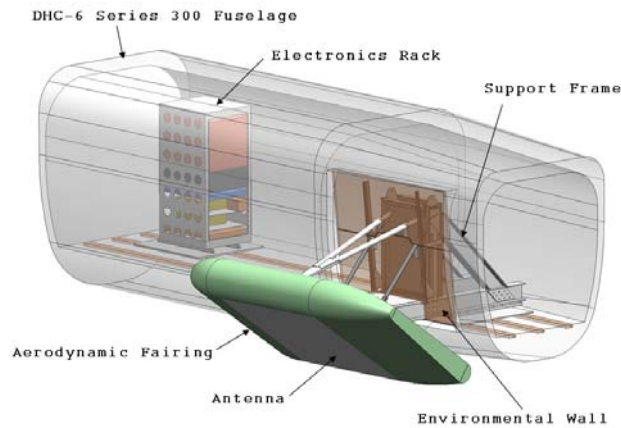


Figure 2. Cryospheric Advanced Sensor (CAS) instrument configuration for technology demonstration on-board a Twin Otter aircraft – A UAV test-bed aircraft.

(Figure 1). Using this model we investigated the characteristics of the ACF/FCF which relate information about the sea ice thickness [1], [3]. Inversion techniques such as genetic algorithm, gradient descent, and least square methods are developed to derive sea ice thickness from the phase information related by the correlation functions [1-3]. Use of two narrow-band radar signals with slightly offset center frequencies for characterizing the ACF/FCF may alleviate VHF frequency allocation restrictions that preclude the use of very wide-bandwidth radar, e.g. as in wide bandwidth sounding radars. This technique also allows suppression of volume scattering effects, which can interfere with ice thickness retrieval.

Prototype VHF radar has been developed for operation on a Twin Otter aircraft for technology demonstration [3], [5], and investigation of the ice thickness retrieval techniques (Figure 2). Testing will be carried for diverse Arctic ice cover conditions. We anticipate that exercising the CAS prototype system over a variety of sea ice conditions will demonstrate the utility of CAS products for application to studies of climate and ocean circulation in the polar region. Although not addressed in the current prototype, future addition of a high frequency, e.g. Ku-band, radar to the CAS instrument package would allow simultaneous measurement of the snow cover, allowing full characterization of the sea ice and snow cover medium.

2. SCIENCE MOTIVATION AND BACKGROUND: AN OVERVIEW

2.1 Sea Ice

The Arctic sea ice cover is a thin veneer with an average thickness of only a few meters. This floating ice cover is in constant motion, driven by winds and ocean currents, often drifting tens of kilometers per day. The ice cover provides a barrier to the exchange of heat and moisture between the atmosphere and the ocean.

The Arctic sea ice cover is both a harbinger and amplifier of climate change. Climate simulations from general circulation models indicate the impact of global warming will be most pronounced in the Arctic. Warming-induced changes in the sea ice can impact global climate through the ice albedo feedback. During winter, the high ice albedo reflects most of the incoming radiation. As the ice cover melts, the highly absorbing ocean replaces the highly reflecting sea ice. Thus more heat is absorbed by the system, resulting in more melting, further lowering the albedo, and putting even more heat into the ocean system. This positive feedback mechanism can amplify small perturbations to the climate system into major changes.

Another critical characteristic of the ice cover is its tremendous amount of spatial and temporal variability. In many ways variability both in horizontal and vertical dimensions is a defining attribute of the sea ice cover. There is spatial variability both in the horizontal and in the vertical. Over short horizontal distances of several meters the ice thicknesses can vary from open water to ridges 10's of meters thick. There are also small-scale changes in the ice structure. Because of the brine entrapped in the ice during freeze-up, changes in ice temperature also cause changes in ice physical properties. Temporal changes in the ice cover are most notably manifest in the annual melt/freeze cycle, with the extent of ice cover varying dramatically with season (Figure 3). During winter, the ice fills the entire Arctic basin and also extends along the coasts of Greenland, the East Coast of Canada, the Bering Sea, the Sea of Okhotsk, and the Bay of Bothnia. In the summer, the ice retreats to the interior of the Arctic basin, with its extent reduced roughly in half. In recent decades, results derived from passive microwave remote sensing techniques have shown a steady decline in the ice area of roughly 3 percent per decade [8]. In addition, the ice cover has been found to be thinning [9-10]. These findings may be harbingers of considerable climate change.

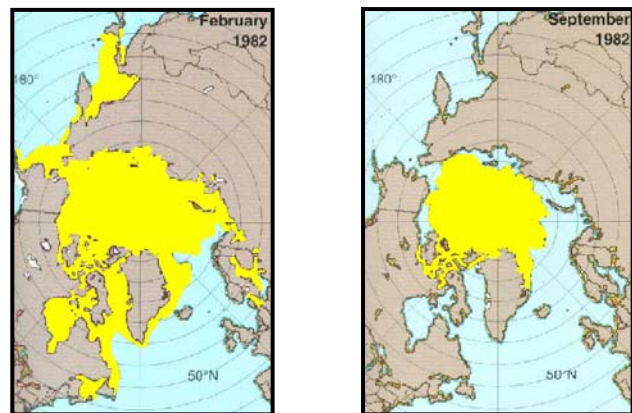


Figure 3. Seasonal variability of ice extent derived from passive microwave remote sensing. Displayed is the winter maximum and summer minimum in 1982.

2.2 Snow Cover

For much of the year, sea ice is covered by snow [11]. Figure 4a shows observations of snow depth, averaged over a 500-m-long line made during the yearlong drift of Ice Station SHEBA in the Beaufort Sea in 1997-1998 [12, 13]. Snow begins to accumulate during freeze up, which typically occurs in August. Snow depth increases rapidly from August through November, then more slowly for the rest of the winter. In the Arctic basin, snowmelt usually begins in early to mid-June, with most of the snow melting in only a few weeks. The decreases in snow depth in Figure 4a were caused by redistribution of snow by wind transport. Some snow loss also occurs due to sublimation.

Figure 4 shows significant spatial variability in snow depth. Over horizontal distances of tens of meters, snow depths can vary from a few centimeters to more than a meter. Blowing snow is quite common in the Arctic and tends to cause snow to collect in rough ice, particularly on the side of pressure ridges.

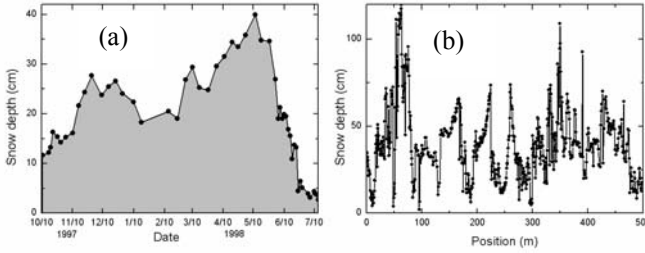


Figure 4. Seasonal evolution and spatial variability of snow depth measured during the SHEBA field experiment. A time series of snow depth averaged over a 500-m-long line is presented in Panel A. Individual snow depths measured every meter along this line on 12 May 1998 are plotted in Panel B. Snow depths are near maximum annual values in May.

Sturm et al. (2002) [13] established that snow depth depends in part on the ice surface roughness. Four ice classes were defined in terms of the ice topography, the surface roughness, and the ice appearance. In increasing order of roughness and snow-holding capacity, the classes were: 1) smooth ice (mostly refrozen leads and undeformed first-year ice), 2) multi-year ice containing large refrozen melt ponds and slightly rougher first year floes, 3) hummocky multi-year ice floes with and without small melt ponds, and 4) deformed ice (rubble fields and ridges). Statistical tests show that at the 90% confidence level, the snow depth differed across all four classes of ice with the exception that no significant difference existed between classes 2 and 3 (refrozen ponds and hummocky ice floes). For the standard deviation of depth, the differentiation by class was not as distinct; only the deformed ice class (ridges and rubble fields) could be differentiated from the other three.

3. SEA ICE MODEL

Sea ice is modeled as a four-layered medium which consists of discrete air, snow, ice and seawater media (Figure 5). The snow and seawater media are assumed homogenous. The sea ice layer consists of a homogeneous ice host with air bubble and brine inclusions. Table I provides the electrical properties of each layer of the medium and the rough surface characteristics of each interface used in our calculations. The three interfaces of air-snow, snow-ice and ice-ocean are modeled as rough surfaces. In addition, the volume scattering effects due to inclusions in the snow and ice layer may become important if the boundaries are smooth. During melt, the snow layer may contain a mixture of air and liquid water as the background material known as ‘wet air’. Based on the published reports [14], [15], typical estimated parameters of these four layer structures are shown in Table 1. The electromagnetic model presented in this paper is parameterized using these values.

The dielectric constants shown in Table 1 are the result of the Maxwell-Garnett mixing formula [16]

$$\epsilon_{eff} = \epsilon_1 \frac{1 + 2fy}{1 - fy}, \quad y = \frac{\epsilon_2 - \epsilon_1}{\epsilon_2 + 2\epsilon_1} \quad (1)$$

Where ϵ_{eff} is the effective dielectric constant, ϵ_1 is the dielectric constant of the background medium, ϵ_2 is the dielectric constant of the inclusions, and f is the fractional volume occupied by the inclusions. Brine inclusions are the dominant inclusions affecting the dielectric constant of bulk sea ice as brine has a large dielectric constant in both real and imaginary part, relative to the ice background. We assume a fractional volume of up to 1.4 % for brine inclusions. Table II lists the constitutive parameters of the air bubble and brine inclusions assumed for sea ice.

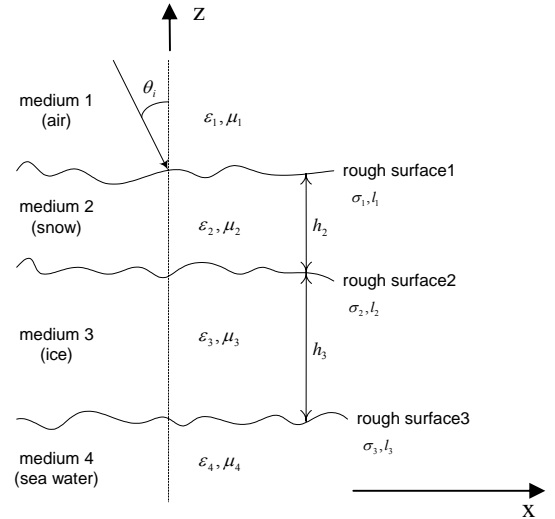


Figure 5. Geometry of the multi-layer model employed for formulating the radar backscatter model.

Table I. Parameters of the background media for parameterizing the backscatter model

	Index of refraction	Layer thickness	Rms Height (cm)	Correlation length (cm)
Layer 1 snow	$\epsilon_2 = 3.15 - j0.001$	$h_2 = 8\text{cm}$	$\sigma_1 = 0.024$	$l_1 = 0.12$
Layer 2 ice	$\epsilon_3 = 4.0395 - j0.4329$	$h_3 = 2\text{ m}$	$\sigma_2 = 0.28$	$l_2 = 1.8$
Layer 3 sea water	$\epsilon_4 = 57.9 - j39.8$		$\sigma_3 = 0.9$	$l_3 = 24$

Table II. Constitutive parameters of the inclusions within the sea ice layer

	Radius	Fractional volume	Dielectric constant
Air bubbles	0.5044 mm	4.3%	1
Brine inclusions	0.1276 mm	1.39%	60-j40

The correlation function is calculated from the constitutive parameters of the sea ice medium using a simple scattering model. For modeling purposes, we assume volume and surface scattering processes are independent. Since the interfaces between layers are smooth relative to the radar wavelength, as is typical for first year ice, the small perturbation method (SPM) is employed to model the contribution of surface scattering processes to the correlation function [17]. For cases where the surface rms height and correlation length are large relative to the wavelength we can use the Kirchhoff approximation for surface scattering. In [1], we present the one-dimensional model based on the small perturbation method (SPM), and in [3] we presented two-dimensional Kirchhoff approximation model and SPM in details. Here, we present the two-dimensional SPM model. The inclusions in the ice layer are very small compared to the wavelength. Therefore, we can use Rayleigh approximation for volume scattering.

4. SCATTERING CONTRIBUTION TO THE CORRELATION FUNCTION

Consider an incident field with Gaussian taper function impinging upon the top of the ice multilayer model shown in Figure 5:

$$\vec{E}_{inc} = \vec{E}_i \sqrt{W} \quad (2)$$

where E_i is the coherent wave field at the top of the snow layer, and W is the illumination function over the surface and is given by

$$W = \exp \left[-\left(\frac{x^2}{L_x^2} \right) - \left(\frac{y^2}{L_y^2} \right) \right] \quad (3)$$

L_x and L_y is the illumination length of the wave in x-direction and y-direction, respectively. We separate the EM wave propagating in the medium into coherent and incoherent waves. The formulation of the correlation function follows.

A. Coherent Component

For the coherent wave, we use the transmission line model approach in which the boundaries are assumed to be flat and multiple reflections in snow and sea ice layers are included.

This is considered a zeroth-order solution to this multilayer media problem. The expressions for calculating the up-going and down-going wave are given in [1] and [3]. Once the “down-going (ψ_d)” and “up-going (ψ_u)” coherent waves are obtained in layer 1 (air), 2 (snow), and 3 (ice), we can find the incoherent wave induced by the rough surface scattering and volume scattering. The ACF/FCF due to interface 1 (air-snow interface), interface 2 (snow-ice interface), interface 3 (ice-seawater interface), and volume (air bubbles and brine inclusions trapped in sea ice layer) can then be easily calculated [1], [3].

B. Incoherent Component- surface scattering

We use small perturbation method to calculate the rough 2D surface scattering contribution. Consider the rough surface interface between two media (e.g. air-snow) as shown in Figure 5. In general, the scattered waves for plane wave incident can be written as [18]

$$\begin{aligned} \bar{E}_s^{(1)}(\vec{r}) &= \int d\vec{k}_\perp e^{i\vec{k}_\perp \cdot \vec{r}_\perp + ik_z z} iH(\vec{k}_\perp - \vec{k}_{i\perp}) S(\vec{k}_\perp, \vec{k}_{i\perp}) \\ &= -i2k_z H(\vec{k}_\perp - \vec{k}_{i\perp}) S(\vec{k}_\perp, \vec{k}_{i\perp}) \left(\frac{e^{ikR}}{4\pi R} \right) \quad \text{For far field} \end{aligned} \quad (4)$$

$$S(\vec{k}_\perp, \vec{k}_{i\perp}) = \left\{ \begin{aligned} &\hat{e}(k_z) \left[f_{ee}^{(1)}(\vec{k}_\perp, \vec{k}_{i\perp}) (\hat{e}(-k_{iz}) \cdot \hat{e}_i) + f_{eh}^{(1)}(\vec{k}_\perp, \vec{k}_{i\perp}) (\hat{h}(-k_{iz}) \cdot \hat{e}_i) \right] \\ &+ \hat{h}(k_z) \left[f_{he}^{(1)}(\vec{k}_\perp, \vec{k}_{i\perp}) (\hat{e}(-k_{iz}) \cdot \hat{e}_i) + f_{hh}^{(1)}(\vec{k}_\perp, \vec{k}_{i\perp}) (\hat{h}(-k_{iz}) \cdot \hat{e}_i) \right] \end{aligned} \right\}$$

where

$$f_{ee}^{(1)}(\vec{k}_\perp, \vec{k}_{i\perp}) = \frac{(k_1^2 - k^2)}{k_z + k_{1z}} \left(\frac{2k_{iz}}{k_{iz} + k_{1zi}} \right) \cos(\phi - \phi_i)$$

$$f_{he}^{(1)}(\vec{k}_\perp, \vec{k}_{i\perp}) = (k_1^2 - k^2) \frac{k_{1z} k}{k_1^2 k_z + k^2 k_{1z}} \frac{2k_{iz}}{k_{iz} + k_{1zi}} \sin(\phi - \phi_i)$$

$$f_{eh}^{(1)}(\vec{k}_\perp, \vec{k}_{i\perp}) = \frac{(k_1^2 - k^2)}{(k_z + k_{1z})} k_{iz} \frac{2kk_{1zi}}{k^2 k_{1zi} + k_1^2 k_{iz}} \sin(\phi - \phi_i)$$

$$\begin{aligned} f_{hh}^{(1)}(\vec{k}_\perp, \vec{k}_{i\perp}) &= \frac{k_1^2 - k^2}{k_1^2 k_z + k^2 k_{1z}} \frac{2k^2 k_{iz}}{k_1^2 k_{iz} + k^2 k_{1zi}} \\ &\quad \left\{ -k_{1z} k_{1zi} \cos(\phi - \phi_i) + k_\rho k_{\rho i} \frac{k_1^2}{k^2} \right\} \end{aligned}$$

$H(\vec{k}_\perp) = \int_{-\infty}^{\infty} d\vec{r}_\perp e^{-i\vec{k}_\perp \cdot \vec{r}_\perp} h(\vec{r}_\perp)$ is the Fourier transform of the

random height function $h(\vec{r}_\perp)$.

$$\vec{k}_\perp = k_x \hat{x} + k_y \hat{y} = k_\rho \cos \phi \hat{x} + k_\rho \sin \phi \hat{y}$$

For convenience, we write the scattered field equation (4) as a product of two terms $H(\bar{k}_\perp - \bar{k}_{i\perp})S(\bar{k}_\perp, \bar{k}_{i\perp})$. Note that, in general, the scattered field in (4) is a vector quantity containing both TE and TM component. Here, we are interested in a more specific case where $\phi = \phi_i$. Therefore, there is no cross polarization component. As a result, the scattered field becomes a scalar quantity. The correlation taken here is the correlation of waves with the same polarization but different frequencies and angles. Also, the terms k, k_1, k_z, k_{1z} and so on are defined in each rough surface interface (see reference [3]). Now, we have the scattered field formulation from one rough surface. The total scattered waves are combination of rough surface scattering from all the surfaces and volume scattering from inclusions in layers. We further make assumption that these scattering phenomena are uncorrelated. Thus, the correlation of scattered waves is the summation of the correlation of wave from each rough surface and correlation of wave from volume scattering. The total correlation function is given by

$$\Gamma = \langle E_r(\theta, \phi, k) E_r^*(\theta', \phi', k') \rangle = \langle E_{s1} E_{s1}^* \rangle + \langle E_{s2} E_{s2}^* \rangle + \langle E_{s3} E_{s3}^* \rangle + \langle E_{v1} E_{v1}^* \rangle + \langle E_{v2} E_{v2}^* \rangle \quad (5)$$

where s1, s2, and s3 denotes the rough surface 1 (air-snow), rough surface 2 (snow-ice), and rough surface 3 (ice-seawater), and v1, v2 denotes the volume scattering from air bubbles and brine inclusions, respectively. And (θ, ϕ, k) denotes the observation angle of wave 1 with wave number k . Prime quantities are for wave 2.

For rough surface scattering, the correlation of the scattered waves for Gaussian beam illumination is given by [3]

Surface 1:

$$\langle E_{s1}(\theta, \phi, k) E_{s1}^*(\theta', \phi', k') \rangle = 4k_z k'_z \langle H_1(\bar{k}_\perp - \bar{k}_{i\perp}) H_1^*(\bar{k}'_\perp - \bar{k}'_{i\perp}) \rangle S_1(\bar{k}_\perp, \bar{k}_{i\perp}) S_1^*(\bar{k}'_\perp, \bar{k}'_{i\perp}) \frac{\exp(-j(kR_1 - k'R_2))}{(4\pi)^2 R_1 R_2} \psi_{id1}(k) \psi_{id1}^*(k') \quad (6)$$

Surface 2:

$$\langle E_{s2}(\theta, \phi, k) E_{s2}^*(\theta', \phi', k') \rangle = 4k_z k'_z \langle H_2(\bar{k}_\perp - \bar{k}_{i\perp}) H_2^*(\bar{k}'_\perp - \bar{k}'_{i\perp}) \rangle S_2(\bar{k}_\perp, \bar{k}_{i\perp}) S_2^*(\bar{k}'_\perp, \bar{k}'_{i\perp}) \frac{\exp(-j(kR_1 - k'R_2))}{(4\pi)^2 R_1 R_2} \psi_{id2}(k) \psi_{id2}^*(k') T_{21}(k) T_{21}^*(k') \exp(-j(q_2 - q'_2)h_2) \quad (7)$$

Surface 3:

$$\langle E_{s3}(\theta, \phi, k) E_{s3}^*(\theta', \phi', k') \rangle = 4k_z k'_z \langle H_3(\bar{k}_\perp - \bar{k}_{i\perp}) H_3^*(\bar{k}'_\perp - \bar{k}'_{i\perp}) \rangle S_3(\bar{k}_\perp, \bar{k}_{i\perp}) S_3^*(\bar{k}'_\perp, \bar{k}'_{i\perp}) \frac{\exp(-j(kR_1 - k'R_2))}{(4\pi)^2 R_1 R_2} \psi_{id3}(k) \psi_{id3}^*(k') T_{21}(k) T_{21}^*(k') T_{32}(k) T_{32}^*(k') \exp(-j(q_2 - q'_2)h_2) \exp(-j(q_3 - q'_3)h_3) \quad (8)$$

where

$$\langle H_j(\bar{k}_\perp - \bar{k}_{i\perp}) H_j^*(\bar{k}'_\perp - \bar{k}'_{i\perp}) \rangle = \pi^2 \sigma_j^2 l_j^2 L_{xeq} L_{yeq} e^{-\frac{A_{cx}^2 l_j^2}{4}} e^{-\frac{A_{cy}^2 l_j^2}{4}} e^{-\frac{A_{dx}^2 l_j^2}{4}} e^{-\frac{A_{dy}^2 l_j^2}{4}}; \quad j = 1, 2, 3 \quad (9)$$

$$\begin{aligned} A_{cx} &= \frac{1}{2} [\beta (\sin \theta \cos \phi - \sin \theta_i \cos \phi) + \beta' (\sin \theta \cos \phi - \sin \theta_i \cos \phi)] \\ A_{cy} &= \frac{1}{2} [\beta (\sin \theta \sin \phi - \sin \theta_i \sin \phi) + \beta' (\sin \theta \sin \phi - \sin \theta_i \sin \phi)] \\ A_{dx} &= \beta (\sin \theta \cos \phi - \sin \theta_i \cos \phi) - \beta' (\sin \theta \cos \phi - \sin \theta_i \cos \phi) \\ A_{dy} &= \beta (\sin \theta \sin \phi - \sin \theta_i \sin \phi) - \beta' (\sin \theta \sin \phi - \sin \theta_i \sin \phi) \end{aligned} \quad (10)$$

$$\frac{1}{L_{xeq}^2} = \frac{1}{2} \left(\frac{1}{L_x^2} + \frac{1}{(L'_x)^2} \right); \quad \frac{1}{L_{yeq}^2} = \frac{1}{2} \left(\frac{1}{L_y^2} + \frac{1}{(L'_y)^2} \right)$$

and σ_j is the j^{th} surface rms height. l_j is j^{th} surface correlation length. L_{xeq} and L_{yeq} is the illumination area on the surface in x and y-direction, respectively. ψ_d is the incident coherent wave upon the surface computed from transmission line model [3]. T_{ij} is the transmission coefficient from the i^{th} to the j^{th} medium. The magnitude of Eq. (6), (7), and (8) show the well known “Memory line” characteristics of the rough surface [19] and it is related to A_d in Eq. (10). The phase of ACF/FCF is the phase contributions of five terms shown in Eq.(5). The first three terms in Eq.(5) are contributions from surface scattering. The last two terms in Eq. (5) are the contribution from the volume scattering explained in the next section. Note that the phase of ACF/FCF of the surface scattering is independent of surface characteristics (rms height σ , correlation length l). However these surface characteristics dictate which surface is dominant in terms of total phase because, as shown in Eq.(6), (7) and (8), the magnitude of ACF/FCF returned to the receiver depends on the surface characteristics and the amount of wave incident upon each surface, which can be determined by coherent transmission line model explained previously.

C. Incoherent component- volume scattering

For volume scattering, we apply the Rayleigh scattering approximation because the inclusions in the ice layer (air bubbles and brines) are very small compared to the wavelength. We assume that all the inclusions are in ice layer (medium 3), and are spherical particles. The scattered field from a single particle is

$$\psi_v(k) = \frac{\exp(-jkR_1)}{R_1} f(k) \exp(-[\gamma_{3o} - \gamma_{3i}] \cdot \mathbf{r}) \psi_d(k) \quad (11)$$

$$T_{32}(k) \exp(-\gamma_{2oz} \cdot h_2) T_{21}(k)$$

where

$k = \frac{2\pi f}{c} = \frac{2\pi}{\lambda}$ is the free space wave number, R_1 is the far field distance in free space $\gamma_3 = \alpha_3 + j\beta_3$ and $\gamma_2 = \alpha_2 + j\beta_2$ are the modified propagation constants in ice layer (background ice) and snow layer, respectively [3], ψ_d is the incident wave at the top of the ice layer, T_{32} is the transmission coefficient from ice to snow, T_{21} is the transmission coefficient from snow to air, and f is the scattering amplitude of the scatterers.

From contribution of several particles,

$$\psi_{v1}(k) = \int_{V_1} \rho(\mathbf{r}) dV_1 \frac{\exp(-jkR_1)}{R_1} f(k) \exp(-[\gamma_{3o} - \gamma_{3i}] \cdot \mathbf{r}) \psi_d(k) T_{32}(k) \exp(-\gamma_{2oz} \cdot h_2) T_{21}(k) \quad (12)$$

Again, we only consider correlation in the same polarization. For TE waves, the correlation function from volume scattering for Gaussian beam illumination is

$$\langle E_{v1}(\theta, \phi, k) E_{v1}^*(\theta', \phi', k') \rangle = f(k) f^*(k') \frac{\exp(-j(kR_1 - k'R_2))}{(4\pi)^2 R_1 R_2} \psi_{id3}(k) \psi_{id3}^*(k') T_{21}(k) T_{21}^*(k') T_{32}(k) T_{32}^*(k') \exp(-(\gamma_2 + \gamma_2^*) \cdot h_2) \rho \pi L_{seq} L_{yeq} e^{-\frac{A_{dx}^2 L_{seq}^2}{4}} e^{-\frac{A_{dy}^2 L_{yeq}^2}{4}} \frac{[1 - e^{-A_{dz} d}]}{A_{dz}} \quad (13)$$

where d is the thickness of the sea ice layer, and

$$A_{dz} = j\beta(\cos\theta + \cos\theta_i) + 2\alpha - j\beta'(\cos\theta + \cos\theta_i) + 2\alpha'$$

D. ACF/FCF results

We now investigate the behavior of the ACF/FCF using the following parameters:

Wave 1: 137 MHz center frequency with incident angle of 30 degree and observation angle at backscattering direction.

$$(\theta_{i1} = 30^\circ, \theta_{o1} = -30^\circ, f_1 = 137 \text{ MHz})$$

Wave 2: 162 MHz center frequency with varying incident angle and observation angle. ($\theta_{i2} = -\theta_{o2}$, $f_2 = 162 \text{ MHz}$).

Layer and surface characteristics are listed in Table I at the snow depth of 8 cm and ice layer thickness of 2 m. Here, the ACF/FCF values for each rough surfaces and volume scattering are normalized to the total ACF/FCF. The magnitude of the normalized ACF/FCF as function of the incident and observation angles of the second wave are shown in Figure 6 which shows the memory line for the rough surface 2 ACF/FCF (top) and 3 (middle), and the memory dots for the volume scattering ACF/FCF (bottom). The dominant contribution is found to be from the ice-seawater (bottom) interface.

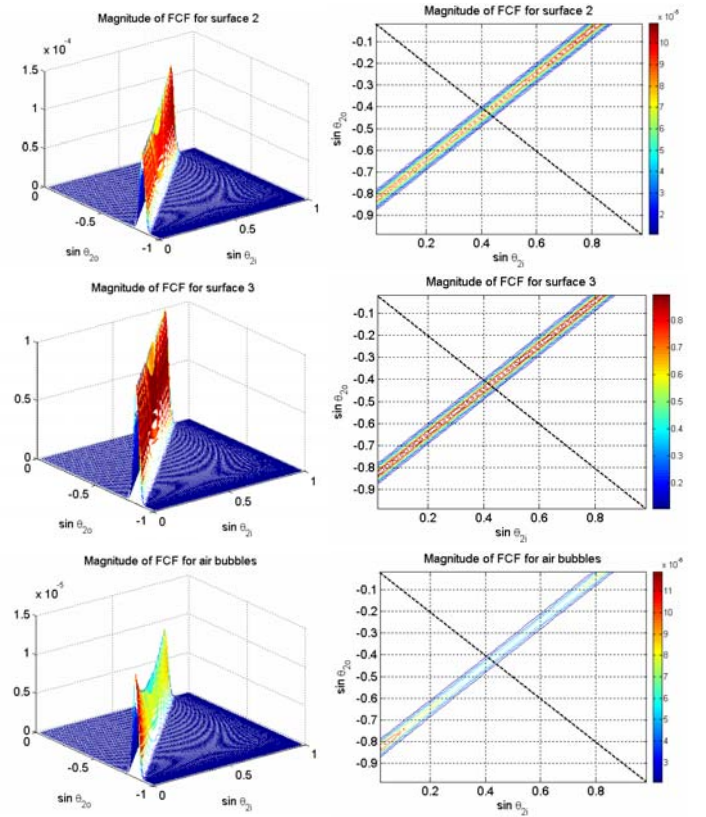


Figure 6. Correlation function for rough surface, top surface 2, middle surface 3, and bottom volume scattering (air bubbles).

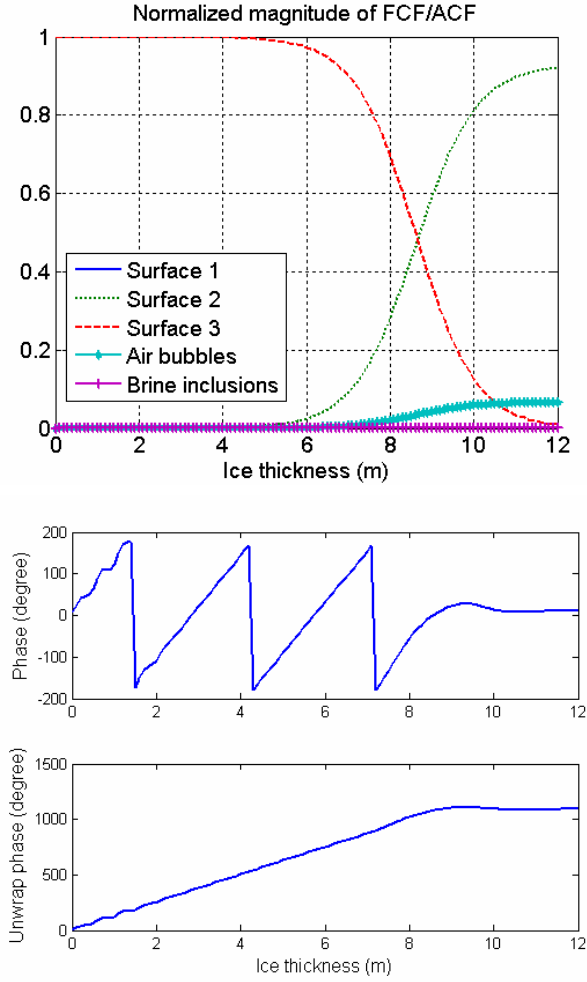


Figure 7a. Amplitude (top) and phase (bottom) of ACF/FCF as a function of ice thickness.

In order to extract information about the thickness of the ice, we need to obtain sufficient amount of scattering from the bottom interface (ice-seawater interface). To maximize the desired surface scattering and to minimize the volume scattering effects, we can choose appropriate combinations of incident and observation angles for both waves as shown in Figure 6.

Figure 7a shows the amplitude and phase of the ACF/FCF as a function of the ice thickness. We use correlation of wave one of frequency of 137 MHz, incident angle of 30 degree and observation angle in the backscatter direction, with wave two of frequency of 162 MHz, incident angle of 25 degree and observation angle in the backscatter direction. These frequencies and incident and observation angles lie in the memory line where the effect of the volume scattering is mostly suppressed.

In this example, the phase of ACF/FCF is linearly related to the ice thickness, for thicknesses up to 9m. Beyond 9m, the phase is independent of ice thickness. This is due to the attenuation within a sea ice layer becoming significant as the ice becomes thicker than 9m. The return signal from the sea ice-water interface, attenuated through the ice layer, becomes significantly less than the return signal from the

snow ice interface. According to our model, utilizing the previously stated surface parameters, the contribution from surface 2 (snow-ice) becomes dominant when ice thickness exceeds 9.0 m (Figure 7a). This limitation is strongly dependent on the characteristics of ice and the rough interface between each layer in our model.

Accuracy of the ACF/FCF phase was independently verified with a numerical model using the Finite-Difference Time-Domain (FDTD) technique for 1D scattering [4]. In Figure 7b, the 1D FDTD results are included for reference. The agreement between the FDTD and SPM models is excellent.

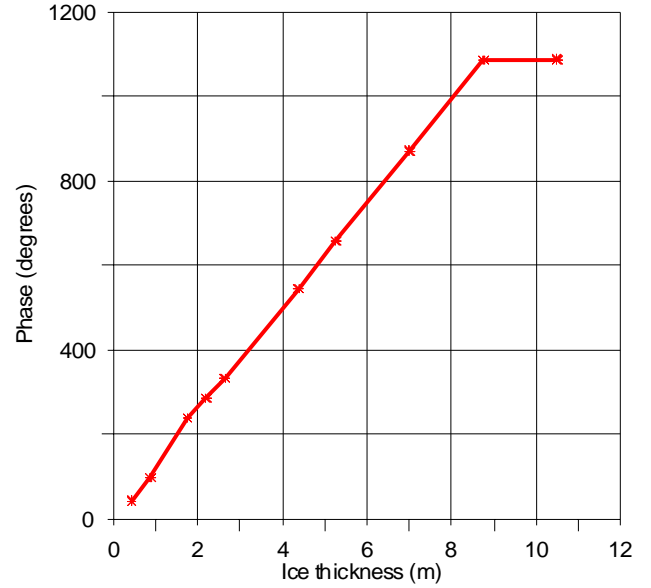


Figure 7b. FDTD phase vs. sea ice depth.

5. Sea ice Thickness retrieval Algorithms

Results from the previous section suggest that the phase of ACF/FCF can be used to estimate the ice thickness. We apply several methods to the ice thickness estimation: gradient-descent (GD), least-square (LSQ) method, and genetic algorithm (GA). Compared with a GD method, and LSQ method, GA does not require the knowledge of the derivative of the ACF/FCF function. Here, we use simulated data from the forward model to make the estimation. In this paper, we present the GA, GD and LSQ results for the 2D rough surface scattering model. The GA, GD, and LSQ results can be found in [1] for the 1D rough surface model.

First, we employ the gradient descent (GD) method to estimate the ice thickness. GD method is to minimize a cost function $(\psi(h) - \psi_m)^2$ where $\psi(h)$ is the phase of FCF calculated from the forward model. ψ_m is the measured phase of FCF, which in this case, we use one simulated data. Let h_0 be the first estimate of the thickness, we can improve the solution by

$$h_1 = h_0 - 2\mu \frac{\partial \psi(h)}{\partial h} (\psi(h) - \psi_m)$$

where μ is the iteration step. This process can be done iteratively until the solution converges within a prescribed margin. Since the phase of FCF (ψ) is a complicated function of height h , we use the numerical derivative.

Second, we apply the least square error concept to the estimation. In the case where we have independent measurements of the ACF/FCF, either by changing combination of frequencies or angles or both, we can apply multiple values and form a minimization problem on the average error. In least square (LSQ) method, we want to find the answer of the equation $(\psi_m - \psi(h_s))^2 = 0$. Starting with an initial estimate h_0 , we can find the increment Δ of the estimate to approach the solution. We have

$$\psi_m - \psi(h_0 + \Delta) = \psi_m - \left[\psi(h_0) + \Delta \frac{\partial \psi}{\partial h} \bigg|_{h_0} \right]. \quad \text{For multiple}$$

data points, we can form a matrix equation. The new estimation of the ice thickness is $h_1 = h_0 + \Delta$. This procedure can be iterated until the solution converges

$$(|h_{new} - h_{old}| \rightarrow \varepsilon).$$

Notice that both GD and LSQ method require a first estimate h_0 . From the formulation of the small perturbation approximation explained in previous section, we can make a few assumptions to derive the first estimation. We assume that the contribution from the snow is small; therefore, we derive the phase of FCF in the case where snow thickness is zero. The expression for h_0 is not shown here due to the space limitations.

The performance of the GD and LSQ method are shown in Figure 8. For GD method, we use wave 1 of 137 MHz with incident angle of 30 degrees and backscatter direction observation and wave 2 of 162 MHz with incident angle of 25 degrees and backscatter direction observation. For LSQ method we include 7 data points using bandwidth of 6 MHz. Measured data are the simulated data from forward model.

Third, we employ a genetic algorithm (GA) optimization approach for sea-ice thickness estimation, h [2],[3]. For GA, we consider a fitness function or objective function for maximization within a constrained range of input parameters h . A binary coding for the parameters h is used. The fitness function is given in Eq (14), and we use it to assign a fitness value to each of the individuals, h , in the GA produce population. In equation (14), $\psi(h)$ is the phase of FCF calculated from the forward model for each

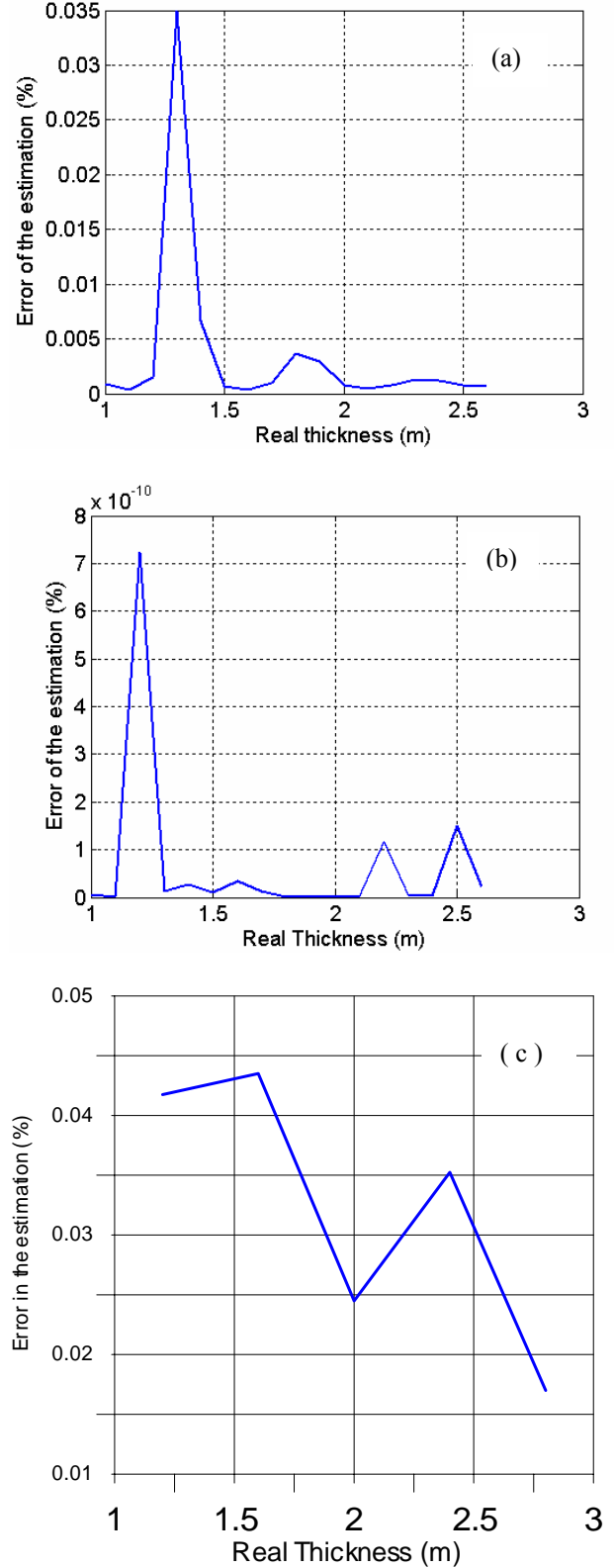


Figure 8. Error of the ice thickness estimation (%) as a function of the true ice thickness. (a) GD method, (b) LSQ and, (c) GA method.

population, and ψ_m is the measured phase of FCF, which in this case, we use, simulated data.

$$fitness = e^{-(\psi_m - \psi(h))^2} \quad (14)$$

Figure 8c shows the error in the estimation using GA for a population of size 10. For a particular trial (real thickness $h=2.0\text{m}$) of this example, a fitness value of $fitness=0.999987$ was achieved after only 11 generations. A near optimal fitness value of $fitness=0.9999947$ was achieved after 47 generations with the parameter $h=2.0\text{m}$.

It should be noted that the results of the optimization shown in Figure 8 depend on the preset convergence conditions and optimization techniques. As an example, the GD minimization of function $(\psi(h) - \psi_m)^2$ and GA maximization of function $e^{-(\psi_m - \psi(h))^2}$ seem to represent the same constraint. However, the condition on the respective convergences may not be the same. The condition on convergence in GD method is placed on the parameter h while the condition on convergence in GA is placed on the fitness function. Therefore, the results in term of the ice thickness retrieval are quite similar in the sense that the estimated thickness is close to the real one, but the error of estimates may be different as shown.

6. FIELD EXPERIMENTAL SYSTEM DESIGN

We have developed a prototype fully polarimetric VHF field experimental radar for technology demonstration, and to investigate the inversion model and its prediction through a sea ice field experiment conducted from an *aircraft on the Arctic Ocean ice cover*. The CAS field experimental system (FES) is designed to accommodate operation from a Twin Otter aircraft, and therefore the antenna size is designed and tailored to an aircraft operation as described below.

A. Radar System Design

To demonstrate the sea ice thickness measurement from the proposed combined spatial and frequency domain interferometer instrument, two separate measurements are required from different altitudes (1.0 km and 1.2 km), with measurements being at offset frequencies and correspondingly different incidence angles. The nominal central frequencies for each measurement are 137 MHz and 162 MHz with 20 MHz bandwidth each, and correspond to the following incidence angles (Figure 1):

Wave 1: $f=162\text{ MHz}$, incidence angle of $\theta_2=25\text{ degrees}$ and observation in the backscatter direction from an altitude of 1.2 Km.

Wave 2: $f=137\text{ MHz}$, incidence angle of $\theta_1=30\text{ degrees}$ and observation in the backscatter direction from an altitude of 1.0 Km.

with a measurement accuracy of better than 5 degrees rms phase noise, and a spatial resolution of 15 meters by 15 meters on the sea-ice surface. The radar system will be configured to sweep over the 127 MHz to 172 MHz frequency range in a 5 microsecond interval for each required altitude measurement. The radar data is sampled at a 480 megasample per second. During data processing, the data will be separated into two separate frequency band channels. The FES radar parameters for the 137 MHz and 162 MHz channel are given in Table 3.

Table 3. CAS radar system parameters

Instrument Parameters			
Center Frequency	137	162	MHz
Chirp Bandwidth	20	20	MHz
Altitude	1	1.2	Km
Transmit Peak Power	100	100	Watts
Pulse Duration	2.22	2.22	usec
Transmit Waveform	CHIRP	CHIRP	
PRF	700	700	
Average Power Radiated	0.155	0.155	Watts
Antenna Radiation Gain	9.0	9.0	dB
Antenna Losses	2	2	dB
Antenna Width	1.1	1.1	Mtrs
Incidence Angle	30	25	Deg
Antenna Length	1.1	1.1	Mtrs
Filtering Losses	1	1	dB
Electronic Gain	70	70	dB
Receiver Noise Temperature	845.5	845.5	DegK
A/D Saturation	-24	-24	dBW
A/D Bits	8	8	Bits
Velocity	46	46	Meter/sec
Sampling Rate (MSPS)	480	480	MspS
Cross Track Resolution	15	15	Meters
Along Track Resolution	15	15	Meters
Number of Looks	7	7	
Boresight Slant Range	1.15	1.32	Km

B. Radar Development and Test

The Cryospheric Advanced Sensor field experimental system is a chirped pulse radar system that operates in the VHF band. Specifically, the system bandwidth is 100 – 200 MHz with the RF chirp generation provided from a 480 MHz direct digital synthesizer (DDS). The block diagram depicting this system is shown in Figure 9a. The radar is shown in Figure 9b.

The transmitter is capable of an output power of 100 Watts and provides a calibration tone for direct input to the receiver. The receiver combines the return signal with the calibration tone at the front-end. The total receiver gain is adjustable in increments of 1 dB ranging from 39 to 70 dB with a total noise figure of 4.5 dB. With the exception of power amplifier and high power switches, the radar hardware is contained within a compact PCI module.

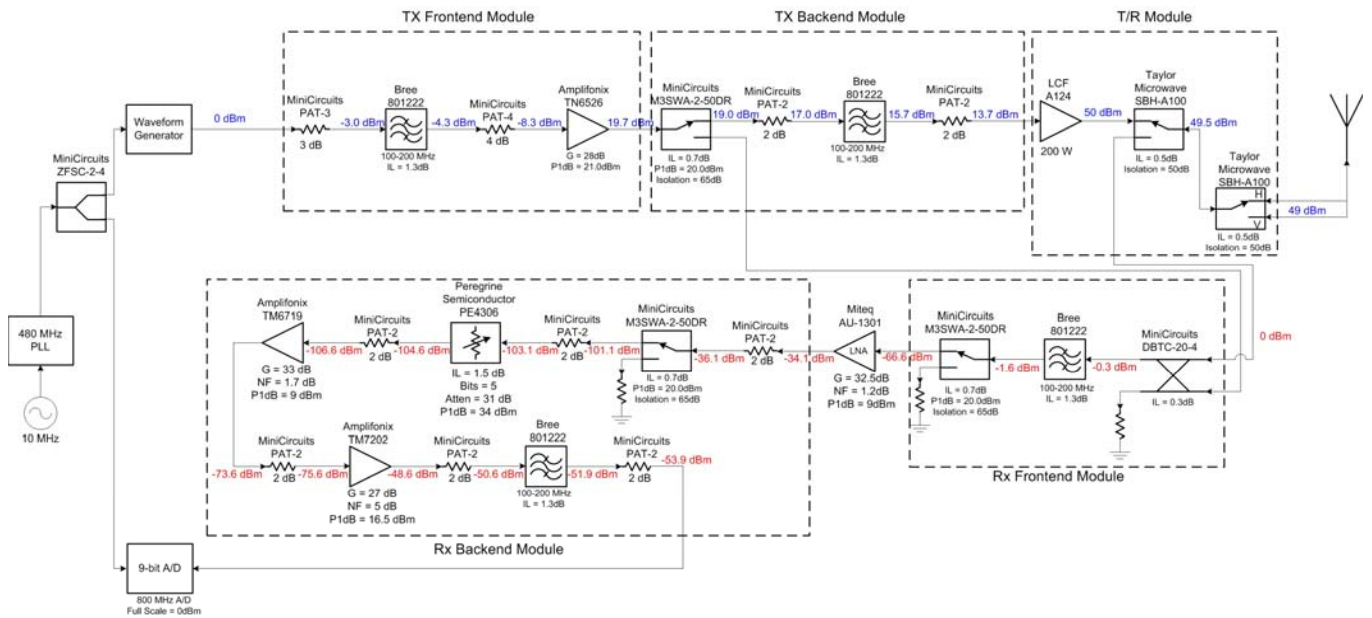


Figure 9a. Cryospheric advanced sensor (CAS) field experimental system (FES) block diagram.

The use of surface mounted RF components made it possible to fit the subsystem into a single slot of a compact PCI chassis. The RF module subsystem is shown in Figure 10a. The module consists of five milled cavities that contain the two transmitter circuit boards, the two receiver circuit boards, and a timing distribution circuit board. The entire compact PCI system is shown in Figure 10b.

A 9-bit, 480 MHz A/D is used to directly sample the received waveform. Both the DDS and the data acquisition module are housed within a single compact PCI card. The PCI interface allows the system to stream data from the digital subsystem to the single board computer and to the hard drive at rates approaching 20 Mbytes/sec. This allows the system to operate at the required PRF of 700 Hz. The software that controls the system is executed on a single board computer running the Linux operating system. The control software is written in C++ and uses QT classes to build the graphical user interfaces.

The FES radar has been laboratory tested end-to-end. During testing, it was verified that the radar was capable of transmitting a 5 microsecond pulse and that the receiver was able to switch to receive mode within 1.6 microseconds after the end of the transmit event. This sequence is necessary to allow operation of the radar from a 1 kilometer flight altitude over ice. Figure 11 below shows the 127-147 MHz- 5us chirp through an 8us delay line. The start time in the plot is the point at which the transmitter begins transmitting the 5us chirp. Approximately 8us later the delayed chirp enters the receiver. The top image in Figure 11 depicts the measured raw data and the bottom image is the pulse compressed image. The pulse compression is done digitally during post-processing. The signal is first down converted to a complex baseband signal before being convolved with a baseband reference chirp.

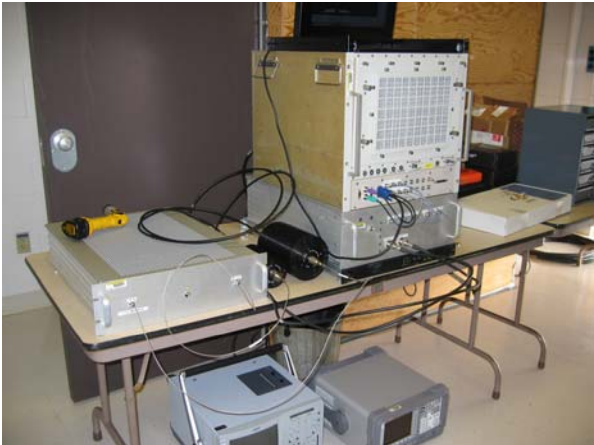


Figure 9b. Cryospheric advanced sensor airborne radar

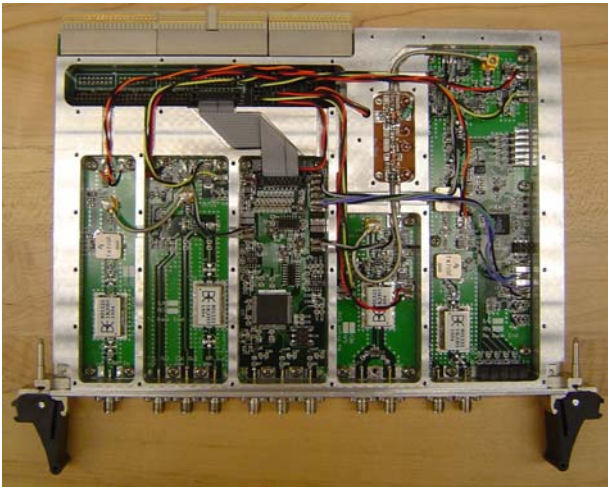


Figure 10a. CAS VHF RF module subsystem.

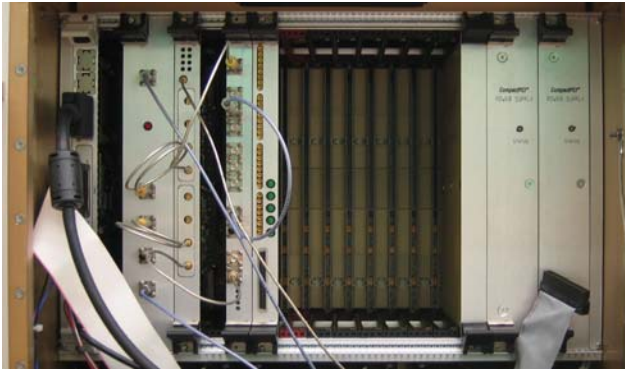


Figure 10b. CAS radar system compact PCI modules

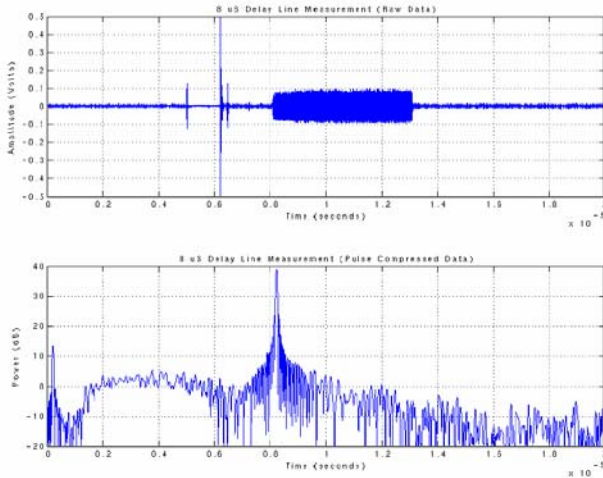


Figure 11. CAS data system window verification: 5us chirp through 8 us delay line.

C. Radar Antenna Design

A dual-polarized and broadband lightweight multi-layer VHF (127-172 MHz) microstrip antenna has been designed, developed, and tested. The antenna with 30% bandwidth has been developed for an aircraft (Twin Otter) field experimental system (FES). This antenna design shown in Figure 12 allows us to acquire two separate measurements from different altitudes (1.0 km and 1.2 km), with each measurement being at separate frequencies.

The antenna will be mounted outside a Twin Otter Aircraft passenger door. The antenna gain is required to be greater than 8 dB so that the FES system is sensitive to the weak backscatter return of the sea-ice sea water interface. The cross-polarization is required to be below 20 dB from the peak of the co-pol. A breadboard antenna element has been fabricated and tested. The antenna has dimensions of 46 x 46 x 14 inches. A four capacitive feeding approach (instead of two orthogonal probes- one for each polarization) for the antenna with 180-degree hybrid connecting the two opposing probes is used to suppress the higher order modes presented in the thick multi-layer antenna substrate (total thickness is 14 inches) as shown in Figure 12b through d.

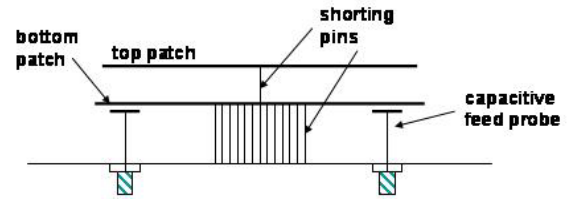


Figure 12a. Side-view of CAS stacked microstrip patch antenna.



Figure 12 (b) Shown is CAS wideband microstrip antenna with its internal shorting pins and four capacitive feed probe. Both top and bottom radiating patches are removed in this photo, (c) antenna front side with radiating patch attached and, (d) antenna backside with two 180- degree hybrids connecting the two opposing feed probes.

This approach allows reducing the antenna cross-polarization level below 20 dB. Twenty-four shorting pins were used on the bottom patch to achieve better than 30 dB isolation between the antenna H- and V-polarization ports (Figure 12b). These four capacitive feeds are attached to the lower resonant (137 MHz) patch layer. The top layer resonates at 162 MHz, and is fed through the energy coupling from the bottom patch layer.

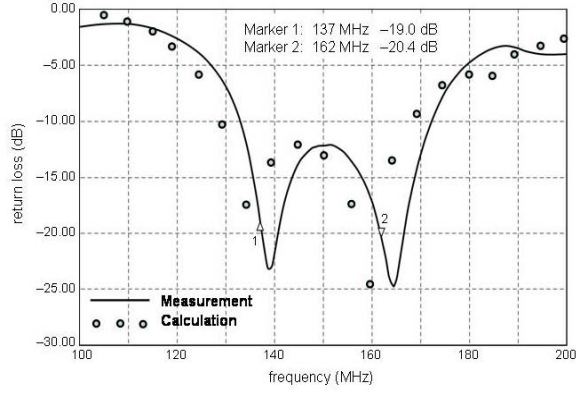


Figure 13. CAS antenna calculated and measured return loss.

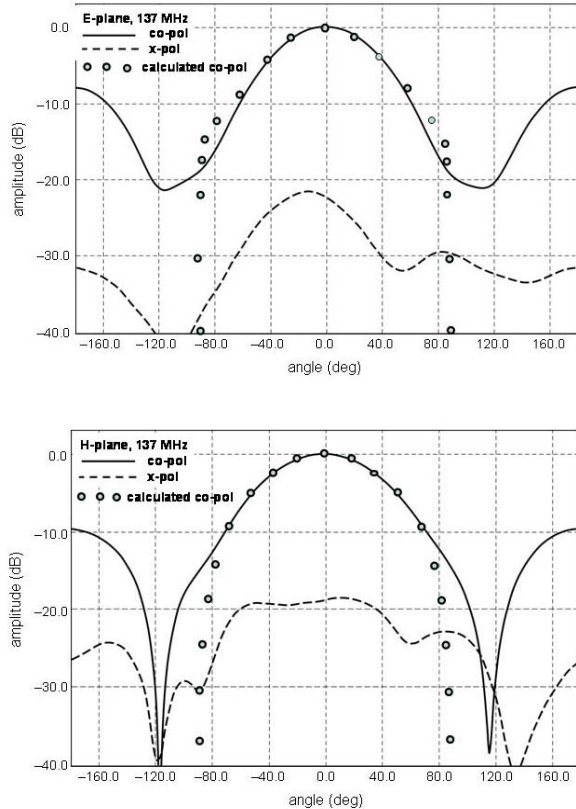


Figure 14a. Measured and calculated antenna E-plane (top) and H-plane (bottom) radiation patterns at 137 MHz.

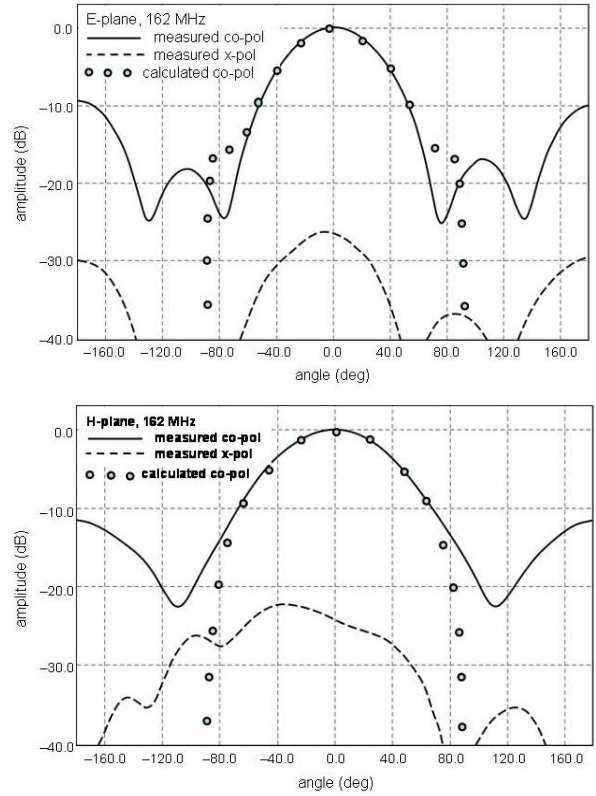


Figure 14b. Measured and calculated antenna E-plane (top) and H-plane (bottom) radiation patterns at 162 MHz.

A wide antenna bandwidth is achieved (127 MHz to 172 MHz), with antenna gain of 8.5 dB at 137 MHz and 10.0 dB at 162 MHz for both polarizations. The calculated and measured return loss results are compared and given in Figure 13. The calculated and measured antenna E- and H-plane patterns at 137 MHz and 162 MHz are given in Figures 14a and b respectively. Excellent agreement between theoretical and measured results is shown for both the antenna return loss (Figure 13) and the radiation patterns over the antenna front hemisphere region (Figure 14).

D. Aircraft Impact on the Antenna Radiation pattern and return loss.

We study the effect of the Twin Otter aircraft shown in Figure 15 on the antenna radiation patterns. The wideband microstrip antenna with and without the presence of the aircraft was simulated using method of moments (MOM). The aircraft was modeled as a perfect electric conductor (PEC) cylindrical structure. The wing and struts are represented by a trapezoidal shape PEC wire mesh (Figure 16). A comparison between the antenna patterns produced model with and without the aircraft show very little effect on the antenna pattern over ± 30 degrees from the peak of the beam. These results are given in [3].



Figure 15. Twin Otter aircraft. The CAS radar will be field tested from a twin Otter aircraft.

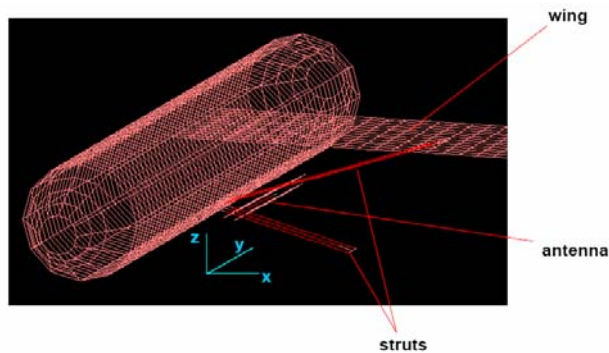


Figure 16. Twin Otter aircraft mesh model for MOM analysis.

E. Radar-Mounted On a Twin Otter- A UAV Test-Bed-Aircraft: Mechanical Design

A DeHavilland Twin Otter DHC-6 Series 300 aircraft, a UAV test-bed aircraft, was selected as the vehicle of choice for carrying the CAS experiment above polar sea ice. This small twin-engine turboprop aircraft is un-pressurized and has a large rectangular doorway aft on the port side. With the doors removed, a frame anchored to the cabin floor is cantilevered out the doorway to suspend the CAS antenna outside the fuselage. An environmental wall covers the doorway opening to preserve cabin temperature and protect occupants, and an aerodynamic fairing surrounds the antenna to reduce drag.

All radar and power electronics are located in a single rack fastened to the aircraft floor inside the cabin (Figure 17). The experiment is operated from input devices mounted to the rack, which also houses an emergency power cut switch and a circuit breaker that will isolate the experiment from the aircraft in the event of an electrical surge. GPS position data is routed to a rack-mounted receiver from an antenna attached to the fuselage. Inertial navigation data is collected by a separate sensor for later correlation to radar data using the GPS timestamp. The electronics and rack together weigh approximately 350 pounds and stand four feet high.

The CAS antenna measures 46 x 46 x 14 inches and weighs 20 pounds. The aerodynamic fairing designed for this shape is nine feet long and five feet wide, built from fiberglass sheets and fabric bonded with adhesives to a foam core. The weight of the fairing is 115 pounds. With the antenna in place it will generate up to 1020 pounds of lift which can act upwards or downwards depending on the angle of attack of the aircraft, and up to 204 pounds of drag at the maximum rated airspeed of 110 knots.

A two-inch thick aluminum honeycomb plate (weights 40 pounds) is bolted to the fairing and fastened to the antenna to provide a backing structure. It attaches to the cantilevered support frame, which is comprised of

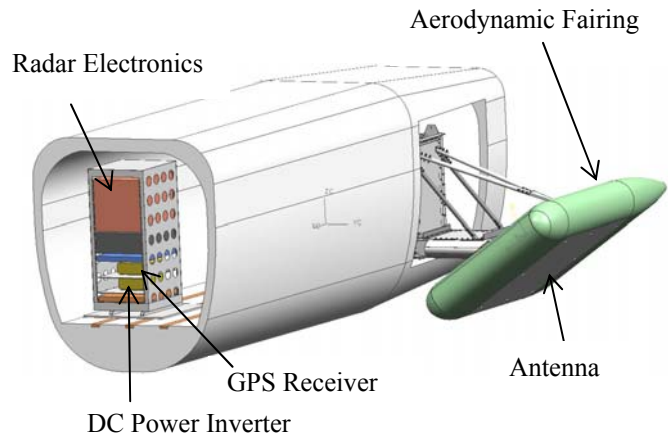


Figure 17. CAS instrument on a Twin Otter aircraft.

4x6-inch extruded aluminum alloy I-beams, shear panels, and tubular support arms. The frame has a weight of approximately 220 pounds and is designed to have first stiffness modes at 22, 27, and 31 Hz with the antenna and fairing attached, considering the estimated compliance of the aircraft floor. This stiffness is sufficient to avoid flutter of the antenna and fairing in the air stream.

Electrical equipment and hardware installed outside the aircraft cabin are designed for structural integrity at temperatures down to -50°C to accommodate extreme conditions that may be encountered in the polar regions. Positive margins with appropriate factors of safety are also shown for the hardware at FAA-defined maximum accelerations of 9g forward, 6g down/3g up, and +/-1.5g laterally to ensure occupant safety. The equipment will be flight tested (June 2005) under an airworthiness certificate in the experimental category prior to operation in the field.

Once installed in the aircraft, the experiment can be operated and flown as conditions permit for a field campaign of one to several weeks duration. Installation and removal are relatively simple tasks, each requiring no more than one day to complete. In addition to the airborne equipment three corner reflectors, each 8 feet on a side and built from perforated aluminum panels, will be transported to the field site, assembled, and installed at locations on the sea ice to provide knowledge of aircraft orientation and the location of ice sampling and measurement sites. The corner

reflectors each weigh about 130 pounds and can be assembled in an hour with minimal tools. Each has been fitted with adjustable support feet and guy lines to secure it in place.

7. SUMMARY

The CAS project is developing reliable technique(s) for direct estimation of sea-ice thickness based on a combined spatial and frequency domain interferometer, and prototyped instrument technology including a demonstration of the instrument capabilities through a sea ice field experiment conducted on the Arctic Ocean ice cover. The CAS project is also conducting a controlled experiment in a laboratory environment for verification of the algorithm and its predictions. The CAS project is also studying various design, technology, and scientific challenges for implementing a cryospheric spaceborne mission, that will combine the frequencies required to determine both sea ice thickness and snow cover characteristics.

ACKNOWLEDGMENTS

The research described in this paper was performed at the Jet Propulsion Laboratory, California Institute of Technology, the University of Washington, Seattle, the University of Kansas, Lawrence, and the US- Army Cold Region Research and Engineering Laboratory under contract with the National Aeronautics and Space Administration.

REFERENCES

- [1] Ziad Hussein, Yasuo Kuga, Akira Ishimaru, Sermak Jaruwatanadilok, and Kyung S. Pak, "Angular and Frequency Correlation for Sea-Ice Thickness Retrieval", IEEE International Geoscience and Remote Sensing Symp. (IGARSS04), Anchorage, Alaska, September 20-24, 2004.
- [2] Ziad Hussein, Yasuo Kuga, Akira Ishimaru, Sermak Jaruwatanadilok, Kyle C. McDonald, Benjamin Holt, Kyung Pak, Rolando Jordan, Don Perovich, and Matthew Sturm, "Determination of Sea Ice Thickness from Angular and Frequency Correlation Functions and by Genetic Algorithm: A Theoretical Study of New Instrument Technology", American Geophysical Union, (AGU), San Francisco, Dec. 13-17, 2004.
- [3] Ziad Hussein, Rolando Jordan, John Huang, Anhua Chu, Benjamin Holt, Kyle McDonald, Prasad Gogineni, Torry Akins, Brandon Heavey, Yasuo Kuga, Akira Ishimaru, Sermak Jaruwatanadilok, Don Perovich, Matthew Sturm, et al "Cryospheric Advanced Sensor: A Spaceborne Microwave Sensor For Sea Ice Thickness And Snow Cover Characteristics", NASA ESTO IIP-3, 2nd year Review Document, January 25, 2005.
- [4] Kyung Pak, Ziad Hussein, Kyle C. McDonald, Seung-Woo Lee, Yasuo Kuga, Akira Ishimaru, and Sermak Jaruwatanadilok, "Numerical Study of Angular and Frequency Correlation Function of Sea Ice at VHF: One-Dimensional Case with the Finite-Difference Time-Domain Method", International Union of Radio Science (URSI), Bolder, Colorado, January 5-8, 2005.
- [5] John Huang, and Ziad A. Hussein, "A Wide-Band Dual-Pol VHF Microstrip Antenna for Sea-Ice Thickness Measurement", International Union of Radio Science (URSI), Bolder, Colorado, January 5-8, 2005.
- [6] Sermak Jaruwatanadilok, Yasuo Kuga, Akira Ishimaru, Ziad A. Hussein, and Kyle C. McDonald, "Snow Thickness Estimation Using Correlation Functions at C-Band", IEEE International Geoscience and Remote Sensing Symp., IGARSS04, Anchorage, Alaska, September 20-24, 2004.
- [7] Benjamin Holt, Ziad A. Hussein, Kyle C. McDonald, and Kyung Pak "A Low Frequency Radar for Direct Measurement of Sea Ice Thickness: Implications of Ice Bottom Surface Roughness", American Geophysical Union, (AGU), San Francisco, Dec. 13-17, 2004.
- [8] Parkinson, C. L., and D. J. Cavalieri, A 21 year record of Arctic sea-ice extents and their regional, seasonal and monthly variability and trends, *Ann. Glaciol.*, 34, 441-446, 2002.
- [9] Rothrock, D. A., Y. Yu, and G. A. Maykut, Thinning of the Arctic sea-ice cover, *Geophys. Res., Lett.*, 26(23), 3469-3472, 1999.
- [10] Laxon S., Peacock N., and Smith D., High interannual variability of sea ice thickness in the Arctic region, *Nature*, 425 (6961), 947-950, 2003.
- [11] Warren, S. G., I. G. Rigor, N. Untersteiner, V. F. Radionov, N. N. Bryazgin, Y. I. Aleksandrov and R. Colony, Snow depth on arctic sea ice. *Journal of Climate*, 12, 1814-1829, 1999.
- [12] Perovich, D.K. et al., Year on ice gives climate insights, *EOS, Transactions of the American Geophysical Union* 80, 481, 485-486, 1999.
- [13] Sturm, M., J. Holmgren, and D. Perovich, The winter snow cover on the sea ice of the Arctic Ocean at SHEBA: Temporal evolution and spatial variability, *Journal of Geophysical Research*, 107 (C10), DOI 10.1029/2000JC000400, 2002.
- [14] F. T. Ulaby, R. K. Moore, and A. K. Fung, *Microwave Remote Sensing: Active and Passive*, Vol. 3, Norwood, MA: Artech House, 1990.
- [15] A. K. Fung, *Microwave Scattering and Emission Models and Their Applications*, Norwood, MA: Artech House, 1994.
- [16] A. Ishimaru, *Electromagnetic Wave Propagation, Radiation, and Scattering*, Englewood Cliffs, NJ: Prentice Hall, 1991.
- [17] A. Ishimaru, *Wave Propagation and Scattering in Random Media*. Piscataway, NJ: IEEE Press, 1997.
- [18] L. Tsung, and J. Kong, *Scattering of Electromagnetic Waves-Advanced Topics*, Wiley-Interscience publications, John Wiley & Sons, Inc, 2001.
- [19] Y. Kuga, C. T. C. Le, A. Ishimaru, L. Ailes-Sengers, "Analytical, experimental, and numerical studies of angular memory signatures of waves scattered from one-dimensional rough surfaces," *IEEE Transactions on Geoscience and Remote Sensing*, Vol. 34, No. 6, pp. 1300-7, 1996.